Extreme Mechanics Letters 43 (2021) 101199

Contents lists available at ScienceDirect

Extreme Mechanics Letters

journal homepage: www.elsevier.com/locate/eml

Interfacial delamination and delamination mechanism maps for 3D printed flexible electrical interconnects

Jacob Brenneman [a], Derya Z. Tansel [b], Gary K. Fedder [a,b,c,*], Rahul Panat [a,*]

[a] Department of Mechanical Engineering, Carnegie Mellon University, Pittsburgh PA 15213, United States of America
[b] Department of Electrical and Computer Engineering, Carnegie Mellon University, Pittsburgh PA 15213, United States of America
[c] Robotics Institute, Carnegie Mellon University, Pittsburgh PA 15213, United States of America

ARTICLE INFO

Article history:
Received 17 November 2020
Received in revised form 13 January 2021
Accepted 26 January 2021
Available online 6 February 2021

Keywords:
Flexible electronics
Heterogeneous materials
Interfaces
Parametric fracture model
Vapor pressure
Delamination
Printed electronics
High temperature

ABSTRACT

Flexible electronic systems integrate heterogeneous materials such as ceramics, metals, and elastomers, which results in interfaces prone to delamination under stress. In this research, we show that delamination can be initiated in a polyimide-based flexible interconnect system directly printed on a polydimethylsiloxane substrate where the metallic interconnect acts as the crack initiation site. This problem is experimentally and analytically evaluated to identify the controlling parameters and propose pathways to prevent delamination. The driving force for delamination is shown to be the vapor pressure of the absorbed moisture in the polymer. Based on the dimensions of the cracks in our system (20–60 μm) and the thickness of the delaminated polymer films (2–6 μm), nonlinear von-Kármán plate theory is utilized to capture both membrane stretching and thin plate bending behavior in the polymer films. The model yields 'delamination mechanism maps' that relate the energy release rate to the geometric dimensions of the flexible interconnects/circuits. For thin polymer films, a 'vapor starved' regime is shown where insufficient moisture reduces the driving force for delamination. For thicker films, a higher resistance to fracture is observed due to an increased rigidity of the polymer layer which behaves as a 'plate' rather than a 'membrane'. Under these conditions, however, the higher retained moisture in the thicker films sustains the driving force for fracture capable of reaching the critical energy release rate. The mechanism maps also reveal the width of the metallic conductor (i.e., the initial crack size) as an important factor controlling fracture. For example, it is shown that the energy release rate for fracture is reduced from 20.5 to 4.6 J/m^2 when the conductor width is reduced from 50 μm to 30 μm for a polymer film thickness of 6 μm. These predictions are shown to be in reasonable agreement with our experimental observations. A finite element model is also developed and used to further validate the analytical model. The work presented in this paper provides highly important and practical design guidelines for improved reliability of flexible electronic systems.

1. Introduction

Flexible electronic devices are used in emerging areas such as smart textiles [1,2], remote health monitoring [3–5], and soft robotics [6,7]. A key advantage of such devices comes from their mechanical properties which are similar to the human skin/body. For example, conformal and comfortable sensing devices mimicking skin enable long-term health monitoring of sensitive neonates [8], while soft wearable robotics can actively support rehabilitation of complex joints while maintaining full range of motion by mimicking the musculoskeletal system [9]. In fact, soft and conformal wearable sensors are considered to be a major part of the future of health care [10].

Flexible electronic systems consist of thin or thick metallic lines that interconnect its electronic components and are typically encapsulated by a polymer. Patterned metallic conductors have the advantage of being compatible with conventional device assembly techniques like solder reflow to integrate traditional silicon-based sensors and chips into flexible and stretchable electronics systems [11]. Direct printing methods such as aerosol jet, inkjet, and extrusion printing allow precise patterning of the metallic conductors as well as sensors and power components such as temperature sensors [12], ceramics and carbon materials for battery and supercapacitor electrodes [13], and polymers for insulation and support [14]. These direct write methods offer a new fabrication toolbox for flexible electronics that enables elastomers, polymers, metals, and ceramics to be integrated in a given circuit with large numbers of combinatorial possibilities. This freedom, however, also gives rise to heterogeneous interfaces resulting in thermoelastic stresses during fabrication due

* Corresponding authors.
E-mail addresses: fedder@cmu.edu (G.K. Fedder), rpanat@andrew.cmu.edu (R. Panat).

https://doi.org/10.1016/j.eml.2021.101199
2352-4316/

to thermal mismatch [15], and mechanical stress concentration during device operation due to elastic modulus mismatch [16]. In fact, we expect stretchable systems with a large number of electronic components on a compliant elastomer substrate to have accentuated delamination problems when compared to rigid circuits [17–19].

A popular substrate material in flexible electronics is polyimide which has remarkable usable temperature range, and high strength and stiffness [3,4,8,20–22]. However, polyimide is extremely hygroscopic, and the adhesion strength has been shown to depend on the moisture loading of the polyimide [23]. At high temperatures, this moisture has the potential to vaporize within voids at material interfaces to cause delamination. While typical temperature conditions during device operation are low, high temperatures are required during device fabrication to cure polyimide or sinter metallic inks. This has been observed in thermoset polymers in the fabrication and assembly of electronic systems [24–26]. Several models have been developed to describe the delamination initiated at a circular edge [27,28], along a straight line [29–31], and to measure the interfacial adhesion energy [32]. Additionally, models have investigated the role of vapor availability, with one model parametrically describing steam driven delamination at high temperatures by considering a circular blister geometry at point defects [24,25,33]. Given the importance of vapor availability to drive crack growth, blister deformation must be accurately captured for all geometric configurations typical of printed electronics. Nonlinear models are required to capture both the effects of tensile stress developed in very thin membranes and the bending stress developed in thicker films. However, to the authors' knowledge, there has not been a model reported to link vapor availability in a nonlinear straight crack with general applicability to the geometry typical of 3D printed flexible electronic devices that span from thin membrane-like films to thicker plate-like films.

This research was undertaken with two clear aims in mind. First, we wanted to demonstrate the conditions under which delamination failure can happen in highly flexible electronic systems consisting of polyimide-silver interconnects on a polydimethylsiloxane substrate. The focus was on utilizing aerosol jet 3D printing (AJP) to create circuits with different interconnection geometries to identify the conditions under which vapor driven delamination can occur. The second aim was to obtain a mechanistic understanding of this problem by developing a parameterized crack model to develop 'delamination mechanism maps' for flexible electronics; and use this knowledge to provide design guidelines to avoid delamination. To verify the parameterized straight crack model and extend the applicability to meandered geometry, two finite element (FE) models were developed and compared against the nonlinear theoretical model.

2. Experimental methods

Materials: The stretchable electronic system consisted of polydimethylsiloxane (PDMS) base, sintered silver nanoparticles as the conductor, and polyimide (PI) as the encapsulant material (around the conductors) as shown in Fig. 1. The PDMS material (Sylgard 184, Dow Corning Corporation, Midland, MI) was prepared by mixing base elastomer and curing agent at a ratio of 20:1 by weight followed by degassing. The interconnect conductor was fabricated using silver nanoparticle ink (Prelect TPS 50, Clariant, Frankfurt, Germany). The nanoparticle size in the ink was 30–50 nm, while the silver particle loading in the ink was 40 $\pm$ 2 weight %. The ink was diluted with deionized water at a ratio of 3:1 (ink:water) by volume prior to printing. The PI precursor resin (PI 2574, HD MircroSystems, Parlin, NJ) was mixed with N-Methyl-2-pyrrolidone (NMP) as a solvent at a ratio of 2:3 by volume.

Sample Fabrication: The flexible electronic system chosen for this study consisted of a PDMS base, and AJP silver nanoparticle interconnects with different widths encapsulated by top and bottom PI layers. The schematic of the construction is shown in Fig. 1A. First, the mixed PDMS base and curing agent was spin-cast onto a silicon wafer having a polyacrylic acid (PAA) release layer following the procedure outlined in our earlier work [34]. The AJP (AJ 300 Optomec Inc, Albuquerque, NM) was used to print the PI and silver interconnects. The AJP has pneumatic and ultrasonic atomizers that convert the ink into aerosol droplets which is carried to the print head with a carrier gas (N_2). This aerosol laden gas is then focused at the print nozzle using a separate sheath gas, again N_2, capable of focusing the aerosol stream to print features down to 10 μm [35,36] depending upon the nozzle size and gas flow parameters. The nozzle size, carrier gas flow rate, sheath gas flow rate, and atomization method all affect the feature size and quality, and several reports have investigated influence of each of the parameters [37–40]. To print PI, the pneumatic atomizer was used along with a 300 μm diameter nozzle, a sheath gas flow rate of 80–100 sccm, and a carrier gas flow rate of 40–50 sccm. The PI layer was then cured in a vacuum chamber at 1 Torr for 3 h at 300 °C with a rapid temperature ramp rate. These curing/sintering process conditions were the same for each layer and illustrated by Fig. 1B. Silver nanoparticle ink was then printed directly onto the cured PI layer utilizing the ultrasonic atomizer and a 150 μm diameter nozzle, a sheath gas flow rate of 45–50 sccm, and a carrier gas flow rate of 25–30 sccm. After sintering the silver (conditions shown in Fig. 1B), another layer of PI precursor was printed on top of the silver to encapsulate the silver interconnects in PI. The top PI layer was then cured, under the same processing conditions as the bottom PI layer, to complete the fabrication of the stretchable electronic platform. Samples were fabricated with varying the PI thicknesses controlled by the number of overlapping print passes. In total, 21 samples were fabricated with 8 samples each printed with one (2 μm) and three (6 μm) passes of PI, and 5 samples printed with two (4 μm) passes of PI. An SEM image (Quanta 600, FEI, Hillsboro, OR) of the printed bottom PI, silver interconnect, and top PI layer is shown in Fig. 1C, while the profilometer scans (Dektak 3, Bruker Corporation, Billerica, MA) of the individual layers are given in Fig. 1D.

Analytical Model and Finite Element Analysis: Nonlinear von-Kármán plate theory was utilized to model the delamination as will be discussed later. To validate the analytical model, two FE models were developed. The first FE model was designed as a 1:1 comparison with the analytical model to validate the deflection and strain energy results. A 2D analysis was conducted in ANSYS (Ansys Inc., Canonsburg, PA) with boundary conditions shown in Supplementary Information, Fig. S1. The void volume was calculated by summing the deflections of the surface nodes along the crack. Vapor starvation was detected (described in Section 3.3) and the input pressure was iteratively changed until the error of $p_{vs}V$ and n_aRT was less than 0.1%. The deflection of the midline nodes, reaction force in the x direction transverse to the interconnect, and strain energy were outputs of interest. The second model was developed to capture more of the complexities that were not modeled in the analytical model including the presence of the silver interconnect, the meandering geometry, nonlinear material properties, and crack growth. A 2D axisymmetric model was developed with the cracks in a meandering pattern, i.e., a distance 'r' away from the center of the axis around which the meander revolves (Fig. S1). The silver layer was included to match with the profile as shown in Fig. 1D. The interface between the

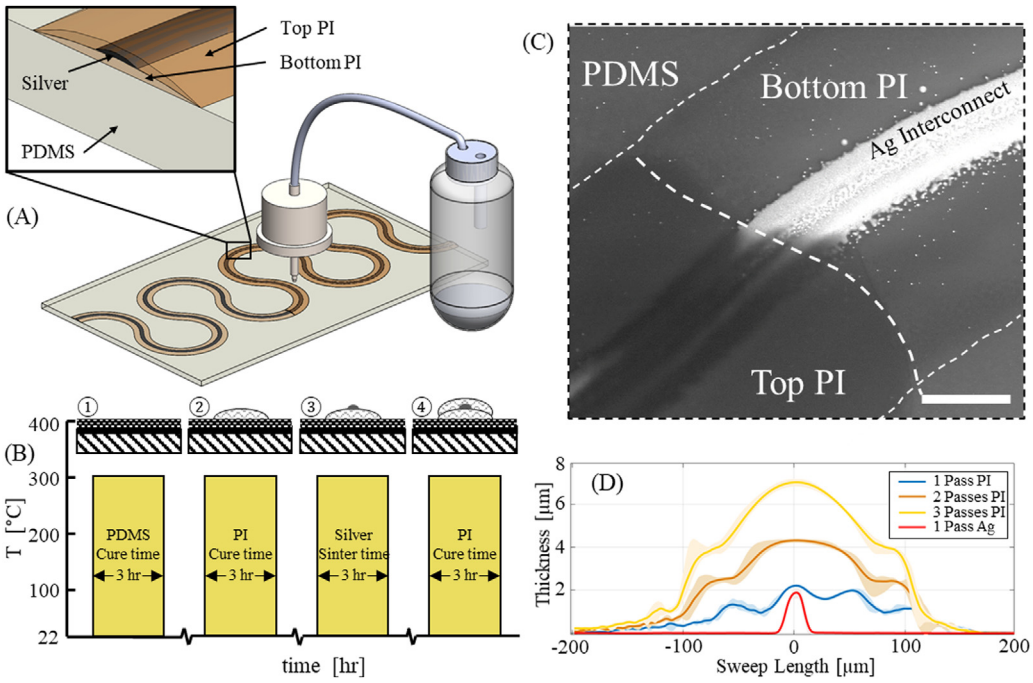

Fig. 1. Schematic of aerosol jet printing with electrical interconnect design and process flow. (A) Schematic of aerosol jet printing where ink is atomized in the vial and carried towards the print head where ink is directly patterned on the substrate. The cross section of the meandering silver electrical interconnect embedded in PI is shown in the inset image. (B) Sintering and curing profiles for each fabrication step (1) spinning PDMS and release layer onto silicon wafer followed by (2) printing of the base layer of PI, (3) printing of silver, and (4) printing of the top layer of PI. (C) Representative SEM image of the PI-encapsulated silver interconnect printed on a PDMS platform. Bar: 50 μm. (D) Profilometer scans on a silicon substrate of a printed silver profile, and printed PI profiles with varied number of printing passes. The solid lines are the average of three scans at different locations along the trace, and the shaded envelope shows the minimum and maximum extent of the scans.

top and bottom layer of PI was modeled with shared nodes that could separate if the critical energy release rate criterion was met. The critical energy release rate is a material property, or in the case of interfacial delamination, a function of the bond strength. The virtual crack closure technique (VCCT) was utilized to calculate the energy release rate, G. The vapor pressure and void volume were calculated at each sub step, and if the vapor starvation condition was met, the simulation was stopped. Both the inner edge and outside edge of the crack were allowed to grow, and the energy release rate for each crack edge was calculated independently, allowing a comparison with the theoretical meander model.

Identical material properties were used in analyzing both the analytical and FE models and are discussed below. For thermoset polymers such as PI, a linear decrease of modulus with increasing temperature up to the glass transition temperature has been reported. Therefore, the elastic modulus of PI at 300 °C was linearly extrapolated from the datasheet and taken to be 1.72 GPa; with a glass transition temperature of 320 °C [41]. The PI moisture uptake was taken to be 2 % from the manufacturer data sheet [42]. Poisson ratio for PI was taken to be 0.34 [41]. The bond strength for two PI layers, both cured at 300 °C, was measured to be 30 N/m using T-peel test [43]. The T-peel test generally includes plastic energy dissipation, in addition to the interfacial fracture. Although the blister delamination modeled in this work is expected to include some plastic deformation, we take the critical energy release rate, G_c, to be 30 J/m ^{2}, which is expected to be the upper bound of the fracture energy. For silver, the Poisson ratio was taken to be 0.37 and an elastic modulus of sintered silver film was taken to be 2.3 GPa from our earlier work [44]. For silver and PI, the tangent modulus was taken to be about 10 % of the elastic modulus.

3. Results and discussion

3.1. Delamination observations

Fig. 2 shows optical and SEM images of the polymer–polymer delamination observed in this work. The delamination was observed between the bottom and the top PI layers, with the silver interconnect in between. As shown in Fig. 2C, the width of the silver interconnect line at the ends of the stretchable circuit was about 50 μm, while that at the center was 30 μm. We observed that the delamination happened only for the section of the circuit where the silver interconnect width was about 50 μm (created by 3 side-by-side passes of AJ printing) and not for a width of 30 μm (created by a single pass) as shown in Fig. 2C. We note that optical images were taken of the samples between every process step (Fig. 1B), and delamination was observed to occur during the cure of the final layer of PI, but only for samples with the thickest PI layers (i.e., with 3 printing passes). Of the 8 samples with the thickest top and bottom PI, a total of three samples showed delamination. For 13 other samples with thinner PI, we did not observe any delamination (see Fig. 2A for a representative SEM image). We also observed that the surface of the silver interconnect (Fig. 2B, also see Fig. 1C) shows characteristic surface roughness due to sintered nanoparticles. The measured profiles of the PI thicknesses are shown in Fig. 1D and were used in the models described later. Fig. 2B shows SEM images of the delamination, with insets showing high magnification images that clearly illustrate polymer–polymer delamination with the silver interconnect in-between.

The polymer–polymer delamination shown in Fig. 2 is observed to occur only for thick PI layers and only at the locations where the metallic interconnects were widest (e.g. Fig. 2C). These observations led us to hypothesize that the silver interconnect acted as the crack initiation sites with the silver width acting

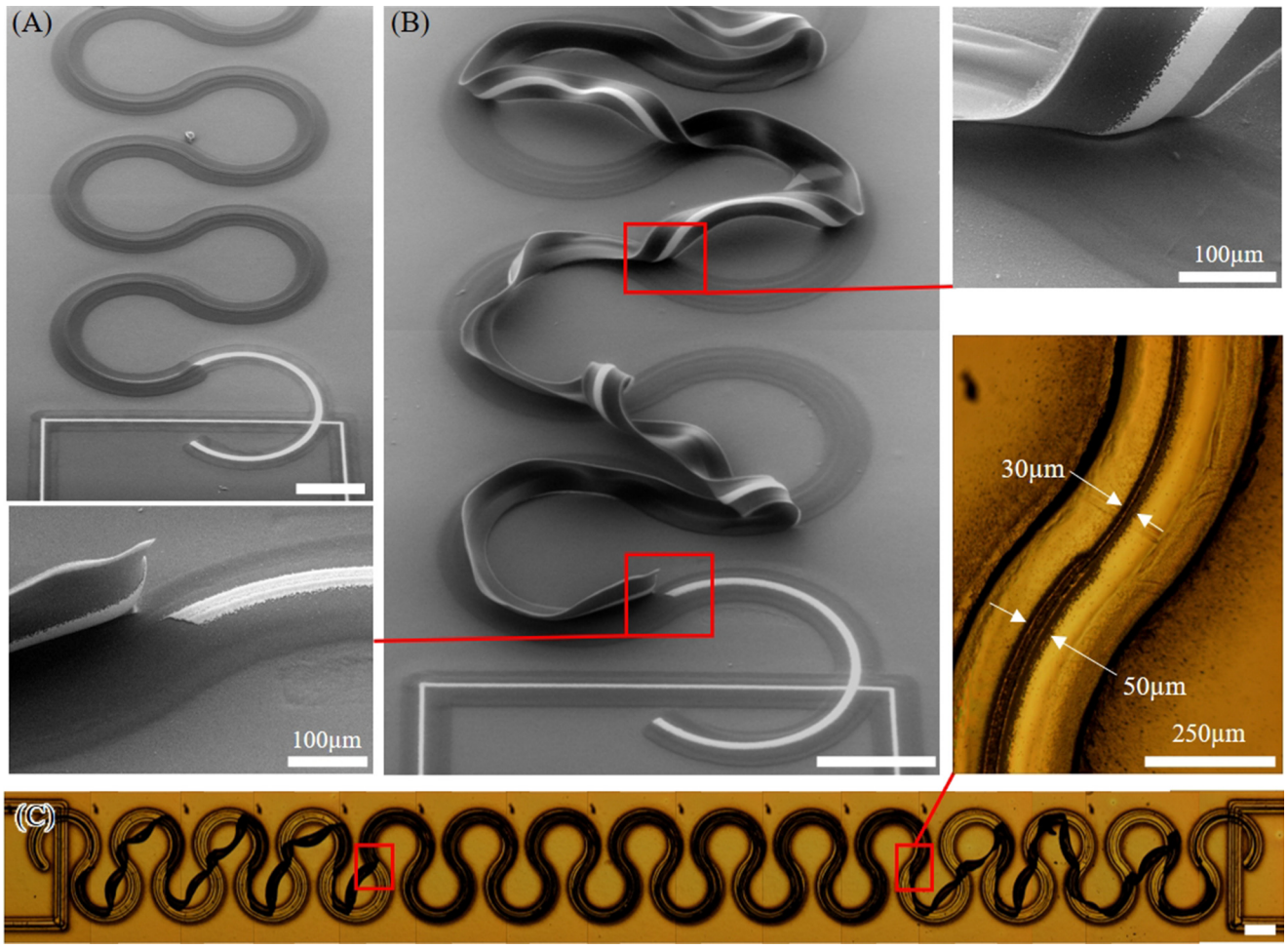

Fig. 2. Delamination between PI layers of prototype stretchable interconnect. (A) SEM image of bonded sample with a single print pass of PI on the top and bottom layers encapsulating the silver. (B) SEM image of delaminated sample with three printing passes of PI comprising the top and bottom layers encapsulating the silver. (C) An optical image, taken after final cure, of the entire printed interconnect. The delamination region is limited to the two ends where the silver trace is 50 μm vs 30 μm wide after the final cure. Inset: transition region from wide to thin silver, image taken before final cure. All scale bars are 500 μm unless otherwise noted.

as the initial crack length. Further, we also hypothesize that the absorbed moisture could diffuse to the PI/silver interface and vaporize; providing the necessary force required for delamination. Thicker PI would allow for a higher level of available vapor and a higher crack driving force. When the critical energy release rate, G_c, is reached, the delamination is expected to occur. Before modeling the system with the above hypotheses (Section 3.3), we investigated the possibility of thermoelastic strain-energy driven delamination in our system (Section 3.2).

3.2. Thermoelastic strain energy model for delamination

The first hypothesis tested was that the cooling of the multilayered interconnect from its curing temperature (300 °C) to room temperature would induce a significant elastic stress due to the thermal mismatch of the multiple materials present in the stack up. This stress can then be relieved when the crack propagates, and the top layer of PI and silver delaminates (Fig. 2B). The strain energy available in the top PI layer and silver layer per delaminated area is then the energy release rate, G. While the energy release rate for thermoelastic strain driven delamination was determined to be insufficient to cause the delamination observed in the interconnects in this work, the thermoelastic model is presented here for use when analyzing interconnects with thicker layers where thermoelastic strain energy may be the dominate driver for delamination. A thermoelastic strain model was developed to determine the strain energy available in the silver and top PI layer assuming a zero-stress state at the curing temperature, thin film assumption, and no applied external forces. The delamination region and the multilayer stack up modeled is shown in Fig. 3A. The model is a 1D model where the thicknesses of the layers, h_i, are varied between the different layers, and the width of the layers, w, and the length of the system, l, are normalized [15]. Each layer experiences a surface force from its neighboring layers as shown in Fig. 3B. Because stack up is not constrained by any external forces, the top and bottom layers only experience an interfacial force from its single neighbor. These interfacial forces are equal biaxial shear forces, and by making a thin film assumption, the shear stress can be assumed to be equally distributed along the length of the stack up and the bending moment inside of the film can be assumed to be small. Then, the shear forces from both neighboring layers can be summed together along the length of the film to determine an equivalent normal force available to elastically strain the layer to match the total strain of the system, ε_{tot}. Each layer has the same total strain ε_{tot} because they are attached, but the elastic strain $\varepsilon_{el,i}$ and thermal strain $\varepsilon_{th,i}$ in each layer are different depending upon the material properties and geometry as described by,

$$\varepsilon_{tot} = \varepsilon_{el,i} + \varepsilon_{th,i} = \frac{F_i - F_{i-1}}{A_i E_i'} + \alpha_i \Delta T \tag{1}$$

where m is the total number of layers, α_i is the coefficient of thermal expansion, ΔT is the change in temperature, A_i is the

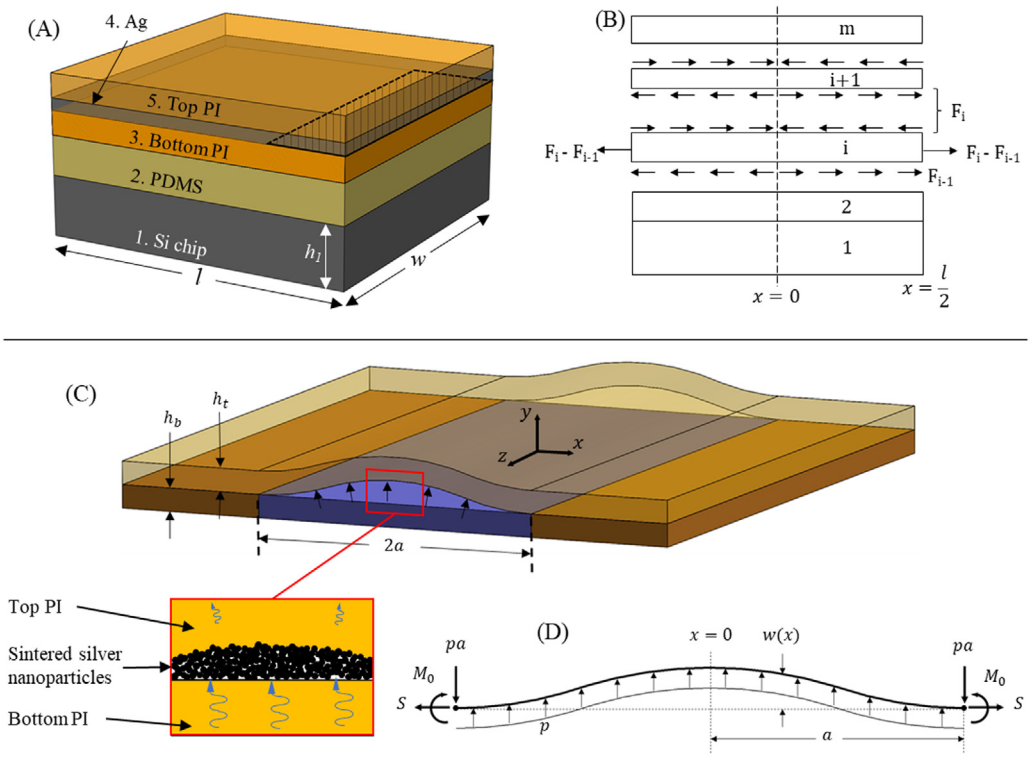

Fig. 3. Thermoelastic and vapor driven delamination model. (A–B) The thermoelastic model has a multilayered stack up (A) matching that of the experimental design with the modeled delamination surface in the hashed area between the Ag and bottom PI layer. (B) Exploded free body diagrams for the layers. The interfacial forces are summed over the length from both neighboring layers to form the equivalent axial force from the assumption that the layers are thin. The interfacial forces arise from the thermal expansion differences of the materials and develop the elastic strain energy in each layer that is available to delaminate the surfaces. (C–D) The vapor driven model consists of the top and bottom layer of PI shown in (C) where the bottom layer of PI is saturated with water moisture. This water moisture is then able to diffuse to the boundary with silver and vaporize in the voids between the rough surface of the sintered silver and the PI as shown in the inset image. The area directly below the delaminated surface (purple region in C) is the volume of saturated PI available to deliver water to the crack void area. The crack is considered to be straight and long in the z direction as shown in (C). The corresponding free body diagram for the vapor driven model is shown in (D) for the deformed state of the top layer of PI. (For interpretation of the references to color in this figure legend, the reader is referred to the web version of this article.)

cross sectional area, $E_i' = E_i/(1-v_i)$ is the biaxial elastic modulus to account for the equal biaxial stress state, and F_i and F_{i-1} are the surface forces of the ith layer. Due to the boundary condition that there are no external forces, F_0 and F_m are equal to zero. The interfacial forces and total strain are unknowns and there are an equal number of equations, allowing the system of equations to be solved to obtain the elastic strain energy in both the top PI layer and silver layer. The energy release rate, G, is then the sum of the change in elastic strain energy of the silver layer and top PI layer [45].

$$G = \frac{\partial U_{Ag}^{el}}{\partial A_d} + \frac{\partial U_{PI}^{el}}{\partial A_d} \tag{2}$$

where

$$\frac{\partial U_i^{el}}{\partial A_d} = \frac{(1+v_i)}{2(1-v_i)} E_i \varepsilon_{el,i}^2 h_i \tag{3}$$

and A_d is the delaminated area.

The full model development and results are shown in Supplementary Information, Section S1. The available energy per unit area for delamination increases linearly with increasing PI thickness as a result of h_i in (3) and is 0.46 to 1.01 J/m^2 for PI having thicknesses of 2 μm and 6 μm, respectively. These values are over an order of magnitude lower than that required for delamination (30 J/m^2) [43]. In a system where the layer thicknesses are significantly larger, the thermoelastic strain energy will play a significant role in delamination. In the current case, however, the available strain energy is unable to drive the experimentally observed delamination. We thus reject the hypothesis that the delamination observed in Fig. 2 is driven by thermoelastic strain energy in the flexible electronic interconnect system.

3.3. Nonlinear von-Kármán plate model for delamination

The hypothesis that the delamination shown in Fig. 2 is driven by vapor pressure in the system was tested with a nonlinear vapor driven delamination model. The model begins by considering the cross section of the meandering interconnects as shown in Fig. 3C. The inset in Fig. 3C shows the top PI layer, the silver interconnect, and the bottom PI layer. Note that PI is a hygroscopic material capable of absorbing 2 % of its mass in water under at room temperature and humidity, and the moisture absorption into the bottom PI layer is expected to be governed by Fick's law [46]. For the length scales investigated in this paper (e.g. Fig. 1D), the absorbed moisture can reach saturation levels at room temperature and humidity within an hour as shown in Supplementary Information, Section S2 and Fig. S3 [24,47]. This time scale is within the range of wait times in our fabrication process shown in Fig. 1C. The moisture from the bottom PI layer directly under the crack surface is assumed to diffuse to the silver interface (i.e. initial crack) at high temperature occurring during the curing stage. Note that at the boundary between the silver interconnect and PI, there are voids due to the surface porosity of sintered nanoparticles as mentioned before, which allow the moisture to vaporize and create pressure at the boundary as shown in Fig. 3C.

We next consider the initial crack surface to be between the silver and the bottom PI layer. This assumption comes from

the experimental observation of the crack interface observed in Fig. 2B and this sets up the model shown in Fig. 3D. Because the PI at both sides of the silver along the x direction are fixed, a tensile reaction develops as the thin film is stretched during the bending deformation. On one extreme of the dimensional combinations in our experiments, a wide silver trace (50 μm) with a thin PI layer (2 μm) results in a membrane like behavior where the tensile stresses dominate. On the other extreme, a narrower silver trace (30 μm) with a thick PI layer (6 μm), results in a case where the bending stresses are most significant. To consider both the membrane stresses and the bending stresses, the nonlinear von-Kármán plate theory is utilized to have a unified model for the entire parameter set. Models of this type do not have exact solutions, but Timoshenko [48] provides a near exact solution for this one-dimensional case that requires only a simple root finding numerical method. The membrane stress, σ_m, bending stress, σ_b, and transverse deflection, w, are

$$\sigma_m = \frac{S}{h} = \frac{Du^2}{a^2 h} \tag{4}$$

$$\sigma_b = \frac{12Dy}{h^3}\frac{d^2w}{dx^2} = \frac{12a^2py}{h^3u^2}\left(u\text{csch}\,(u)\cosh\left(\frac{ux}{a}\right) - 1\right) \tag{5}$$

$$w = \frac{pa^2\left(a^2 - x^2\right)}{2Du^2} - \frac{pa^4}{Du^3\tanh u}\left(1 - \frac{\cosh\frac{ux}{a}}{\cosh u}\right) \tag{6}$$

where p is the vapor pressure, a is the half crack length, h is the thickness of the plate, y is the distance from the plate centerline, x is the distance from the blister center, D is the flexural rigidity of the plate, and S is the developed tensile reaction force. The second term in (6) describes the contribution of membrane stresses. The first term of the transverse deflection in (6) is similar to the beam theory result with the addition of the simplifying term, u, described as

$$u^2 = \frac{Sa^2}{D} \tag{7}$$

This term links the flexural rigidity to the developed tensile stress and is dependent on the geometry, pressure applied, and material properties being modeled. The solution for the u term is found by applying fixed boundary conditions at both end points in the x direction. Therefore, the extension of the film by the tensile reaction force S in plane strain is equal to the difference between the length of the deformed curve and the initial crack length $2a$ which is

$$a\varepsilon_m = \frac{Sh^2a}{12D} = \frac{1}{2}\int_0^a \left(\frac{dw}{dx}\right)^2 dx \tag{8}$$

After substituting (6) into (8) and performing the differentiation and integration, (8) can be rearranged into the following relationship.

$$\frac{D^2h^2}{p^2a^8} = -\frac{9}{u^7\tanh u} - \frac{3}{u^6\sinh^2 u} + \frac{12}{u^8} + \frac{2}{u^6} \tag{9}$$

For a given pressure, material, and geometry, u can now be found. While (9) gives an analytical relationship for u, numerical methods such as a root finding method must be used to solve for u in order to get the stresses (4) and (5) and the deflection (6).

The strain energy, U^{el}, can now be found by noting that the stress contributions from (4) and (5) in the delaminating plate are both normal in the same direction and can simply be added together to find the total stress on a differential element. The strain energy density is then integrated over the entire volume to find the strain energy

$$U^{el} = \frac{Dh^3}{12}\int_{\frac{-h}{2}}^{\frac{h}{2}}\int_0^a (\sigma_m + \sigma_b)^2\, dxdy$$

$$= \frac{Dh^2u^4}{12a^3} + \frac{a^5p^2\left(u^2\text{csch}^2u + u\coth u - 2\right)}{2Du^4} \tag{10}$$

The energy release rate, also known as crack extension force, is

$$G = \frac{1}{2}\left(\frac{dU^{el}}{da}\right)_p \tag{11}$$

where U^{el} is given by (10). Eq. (11) can be numerically solved using the finite difference method but does not have an exact solution, because u is dependent upon a. The derivative in (11) may be taken at constant pressure or constant displacement resulting in equivalent energy release rate determinations when the change in crack length is small, but the constant pressure condition is most easily implemented in this case because p appears explicitly in (10).

In vapor pressure driven delamination, the absorbed water is diffused from the bottom layer of polymer to the boundary with the silver and evaporated into the micro voids at high temperature during the final cure step. The ideal gas law can be used to relate the developed pressure and volume per unit length, V, of the void given the temperature, T, and available water molecules.

$$pV = n_aRT \tag{12}$$

where $R \approx 8.314\ \text{J}\cdot\text{K}^{-1}\ \text{mol}^{-1}$ is the ideal gas constant. The total number of absorbed water molecules per unit length available, n_a, to fill the void is assumed to be contained in the bottom layer of polymer directly under the crack area, which is shown in Fig. 3C as the purple region. The total number of absorbed water molecules per unit length available can then be described by geometric terms

$$n_a = 2ah_b\left(\frac{\rho_{poly}wt\%}{M_{molH_2O}}\right) \tag{13}$$

where h_b is the bottom polymer thickness, ρ_{poly} is the density of the polymer, $wt\%$ is the weight percentage of water absorbed, and M_{molH_2O} is the molar mass of water. Vapor pressure will reach saturated steam pressure, $p_{sat}\,(T)$, if there is enough water present. However, if the deflection of the blister is large, the void volume may grow large enough where there is not enough water absorbed in the polymer to reach saturated steam pressure (i.e. $p_{sat}V > n_aRT$). This region is called the vapor starved region, and in this case the pressure will be less than p_{sat} and will depend on the void volume and moisture content under the blister. The void volume of the blister is

$$V = 2\int_0^a w dx = \frac{a^5p\left(u^2 - 3u\coth u + 3\right)}{3Du^4} \tag{14}$$

Combining Eq. (14) with Eq. (12) and solving for p, the pressure in the vapor starved region is

$$p_{vs} = \sqrt{\frac{3Du^4n_aRT}{a^5\left(u^2 - 3u\coth u + 3\right)}} \tag{15}$$

The saturated vapor pressure is simply a function of temperature and can be found in steam tables. The vapor starved pressure, p_{vs}, however, is a function of u, which in turn is a function of pressure and must be found numerically; again, possibly implemented with a root finding method. The internal blister pressure is found for both the saturated and vapor starved conditions:

$$p = \left\{ \begin{array}{ll} p_{sat} & \text{if } p_{sat}V \le n_aRT \\ p_{vs} & \text{if } p_{sat}V > n_aRT \end{array} \right\} \tag{16}$$

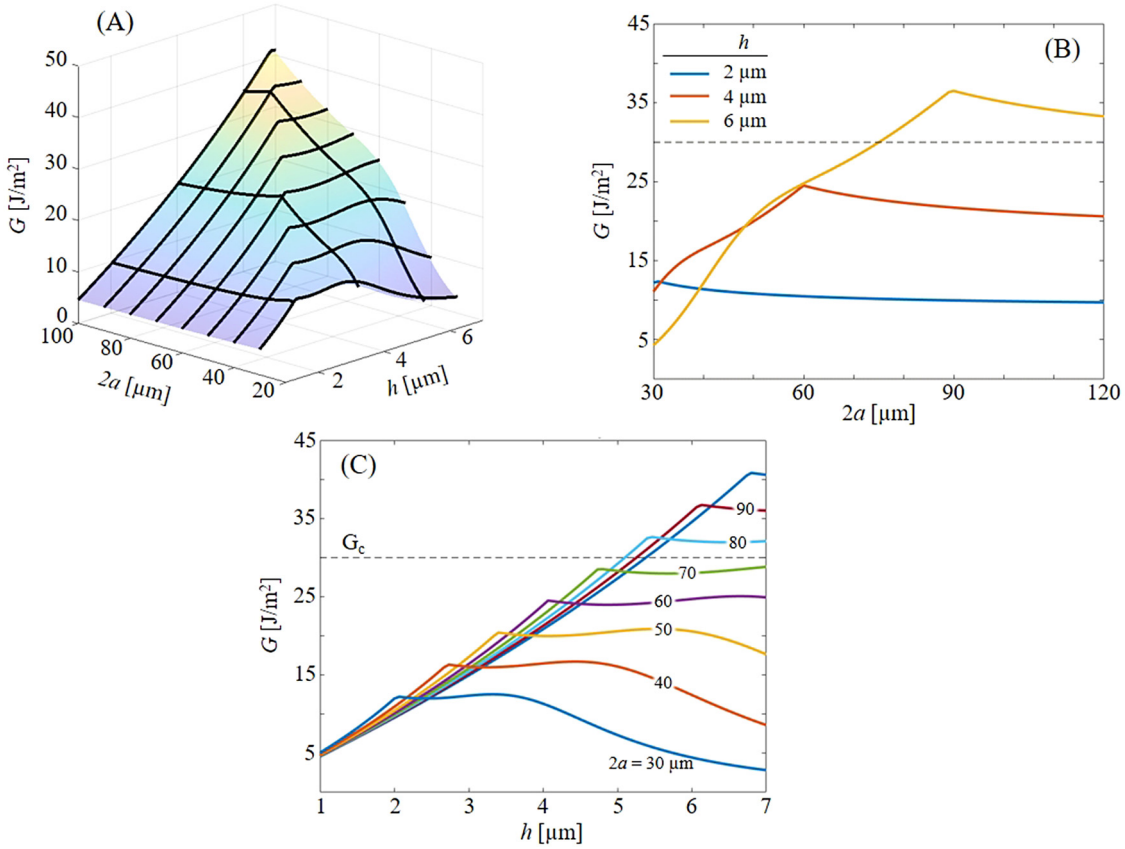

Fig. 4. Energy release rate vs crack length, and PI layer thickness (A) The surface plot shows the mapping of the energy release rate varying both the crack length, in this case 2*a* which is initially the silver width, and the PI layer thickness, where the top layer and bottom layer are the same thickness matching our test samples. (B) Holding the PI layer thickness constant, three curves are shown from the surface plot matching the thickness of the PI in test samples. (C) Holding the crack length constant, the effect of continuously increasing PI layer thickness is shown for various crack lengths, 2*a*.

3.4. Modification of model for serpentine delamination geometry

The model in Section 3.3 assumes that the interconnect is straight, i.e., has an infinite radius of curvature (Fig. 3C). The geometry of the interconnect in our experiments, however, is serpentine (Fig. 2). This geometry is incorporated into our model by considering the difference in energy release rate separately on the inner side of the interconnect (G_i) vs the outer side of the interconnect (G_o). For curved interconnects, the total strain energy contribution to the numerator of (11) increases by a factor of $2\pi r$, due to the out-of-plane dimension being axisymmetric instead of Cartesian (i.e., normalized to unity), with r being the radius of curvature. The differential crack growth area (the denominator of (11)), changes from $2\partial a$ to $4\pi\,(r-a)\,\partial a$ for the crack face on the inner edge of the serpentine, and $4\pi\,(r+a)\,\partial a$ for the crack face on the outer edge of the serpentine. Inserting these values into (11), an estimation of the differences between the inner and outer crack extension forces are:

$$G_i = \frac{2\pi r}{4\pi\,(r-a)}\frac{\partial U^{el}}{\partial a} = \frac{r}{(r-a)}G$$
$$G_o = \frac{2\pi r}{4\pi\,(r+a)}\frac{\partial U^{el}}{\partial a} = \frac{r}{(r+a)}G \qquad (17)$$

3.5. Model prediction and comparison with experiments

Fig. 4 maps the energy release rate, G, as predicted by the analytical model as a function of two critical dimensions of the problem. The first dimension is the PI thickness, which in this case is set equal for both the top and bottom layers. The second dimension is the initial crack length, 2*a*, which is the width of the silver interconnect lines. The black isolines in Fig. 4A represent constant thickness and constant crack length. The crack length and PI thickness isolines are then plotted in Fig. 4B and 4C, respectively.

Fig. 4B shows the energy release rate increasing with initial crack length for both the 4 μm and 6 μm-thick PI. From Fig. 4B, it is interesting to note that only the 6 μm-thick PI sample crosses the critical energy release threshold at a 76 μm crack length, signaling the onset of delamination. This result is consistent with the experimental observation that only samples with thicker PI (6 μm thick) delaminate during the curing of the top layer of PI. In experiments, the samples with a PI thickness of 2 μm and 4 μm did not show any delamination. This strong match between the model and experiments provides confidence regarding the hypothesis of the delamination mechanism as well as the model developed in this work. We note, however, that the delamination threshold is reached at an initial crack length of 76 μm, which is higher than the 50 μm maximum silver width observed in experiments (Fig. 2C). The model shows that the energy release rate for an initial crack length of 50 μm is 20.5 J/m^2. This minor difference between our experimental observations and the model can be attributed to PI thickness variation not captured in model, material property variations from reported values at the specific temperature, and moisture loading of the PI layer. The trend predicted in Fig. 4, however, is consistent with the observed experimental delamination represented in Fig. 2.

In Fig. 4B, the energy release rate reaches a limit and starts decreasing at crack lengths of 59 μm and 88 μm for the 4 μm and 6 μm-thick PI films, respectively. The energy release rate then flattens and converges to a value as the crack length increases.

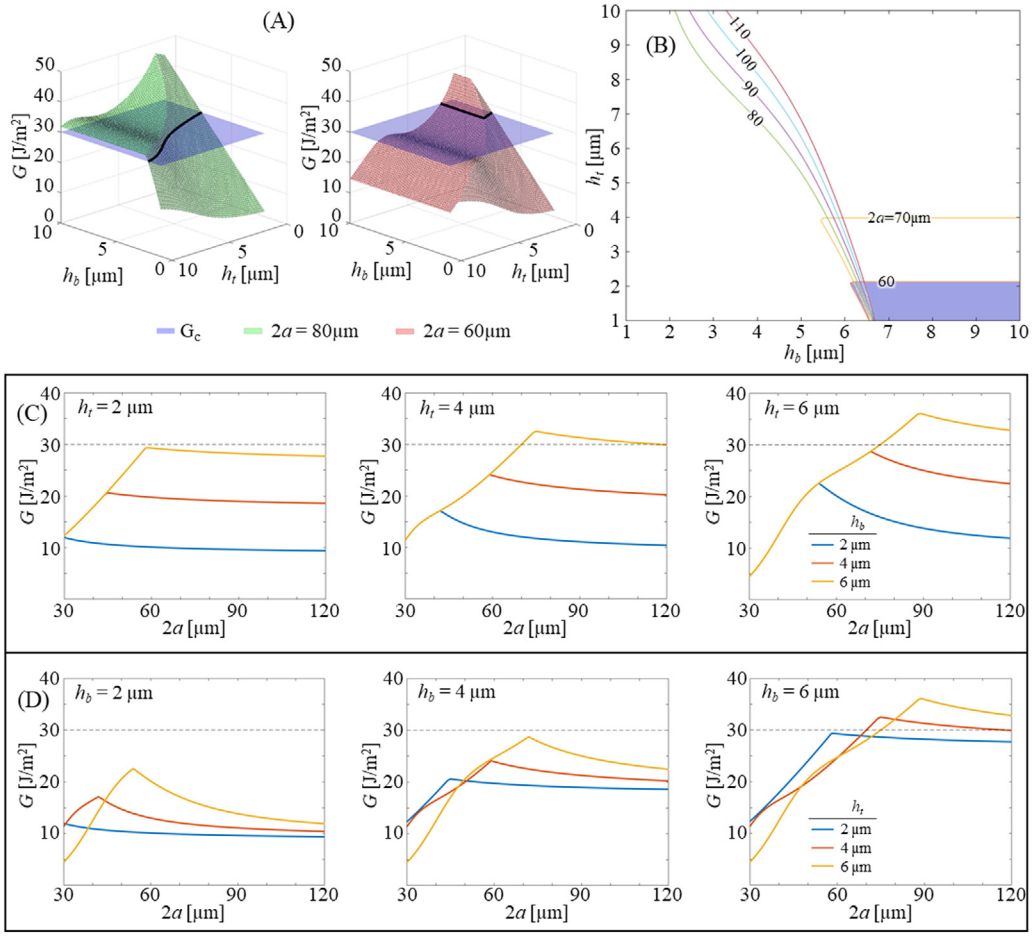

Fig. 5. Delamination Mechanism Maps (A) The surface plots show the mapping of the energy release rate varying both the top and bottom PI thickness for two different crack lengths. The blue surface on both plots is the critical energy release rate of 30 J/m ^{2} and the isolines are highlighted in black at the critical energy release rate. Any portion of the surface higher than the critical energy release rate will delaminate. These isolines are then plotted in (B) for each silver width or crack length ($2a$) to create a design map of regions with and without delamination for all three geometric parameters. The delamination region is highlighted in blue as an example for the 60 μm crack length. (C) Individual graphs hold the top layer of PI constant, while showing curves for three different thicknesses of the bottom layer of PI. (D) Individual graphs hold the bottom layer of PI thickness constant, while showing curves for three different thicknesses of top PI. Part (C) and (D) show the individual effects of the top and bottom PI thicknesses in the vapor starved and vapor rich region along with the critical energy release rate of 30 J/m^2 shown by the dotted line. (For interpretation of the references to color in this figure legend, the reader is referred to the web version of this article.)

This limit is the onset of vapor starvation described by (16), where there is no longer enough moisture to maintain the saturated steam pressure. Reducing the available moisture is then a critical step in reducing the likelihood of delamination by limiting the energy release rate in the vapor starved region. This can be achieved by several methods such as incorporation of a drying step prior to the final high temperature cure, utilizing a polymer encapsulant with a lower moisture update, or by reducing the thickness of the bottom polymer layer.

Vapor starvation occurs at a smaller crack length for thinner layers of PI, as shown in Fig. 4B, for two reasons. First, there is less moisture available for a given crack length, because the bottom layer of PI is thinner and therefore has less total moisture absorbed. Second, the deformation for thinner top PI layer (small h) at the same pressure is larger, creating a larger void for the vapor to fill at the same crack length. This is exemplified by the 2 μm-thick PI, where it becomes vapor starved at 30 μm and converges to a lower energy release rate of approximately 10 J/m^2. Therefore, the top and bottom PI layer thicknesses have different effects on the developed energy release rate and can be investigated independently.

Fig. 5 shows the effect of independently varying the bottom and top PI thicknesses on the energy release rate. The surface map in Fig. 5A shows the energy release rates for two different crack lengths of 60 μm and 80 μm, where the top and bottom PI thicknesses are varied from 1 μm to 10 μm. Both surfaces indicate two distinct regions: the vapor starved region and the vapor rich or saturated region. The vapor rich region is wavy with larger energy release rate and has no dependence on the bottom layer of PI, except to form the boundary where it becomes vapor starved. This is shown in Fig. 5C where the top PI layer thickness h_t is held constant, and three curves for different bottom PI thicknesses h_b overlap until reaching the vapor starvation region. Then, once the vapor starvation region is reached, the energy release rate slowly decreases and converges to a value which is determined largely by the bottom layer of PI. This is shown in Fig. 5D more clearly, where the bottom PI layer thickness is held constant in the three different graphs. The energy release rate in the vapor starved region is nearly independent of the top layer of PI as the curves converge to a single value independent of crack size and top PI thickness. Furthermore, the magnitude of the converged energy release rate in the vapor starved region is only dependent on the thickness of the bottom layer of PI. The energy release rate is then determined by the available moisture to fill the voids and can be limited to a maximum value – independent of crack size – if the moisture loading can be reduced in the bottom layer of PI to the point of vapor starvation.

Fig. 5B represents a delamination mechanism design map linking the three geometric parameters of silver interconnect width, top PI thickness, and bottom PI thickness to the likelihood of delamination of any of those combinations. This delamination map is created from the isolines in Fig. 5A where the surface intersects with the critical energy release rate, signifying the onset of delamination. Additional isolines of critical energy release rate for different crack lengths are plotted in Fig. 5B to complete the map. The area filled in with blue represents conditions where delamination is likely to initiate for crack lengths or silver widths of 60 μm. Design guidelines to reduce the energy release rate can be extracted from this mapping and include reducing the bottom PI thickness to reduce the moisture available, increasing the top PI thickness to increase the mechanical stiffness of the system which results in less strain energy for a given pressure, and printing smaller silver interconnect widths to reduce the initial crack length.

3.6. Validation of analytical model by finite element modeling

The analytical model described in Section 3.3 captured both the bending and tensile stresses developed in thin polymer films/plates arising from a non-linear behavior. The model, however, still makes important assumptions such as small angle approximations, and no contribution from shear stress. While these assumptions are widely made with good results on the maximum stress developed, an accurate deformation result is important for determining the energy release rate in this model. In this section, the results from the FE models (see Methods, and Fig. S1) are compared against the analytical model to investigate the significance of these simplifications. Fig. 6 compares the maximum displacement w_{max}, the tensile vs bending reaction characterized by the parameter u, and the energy release rate, G, between the analytical model and the FE model. The displacement comparison in Fig. 6A shows that the analytical model captures the nonlinear behavior shown by the FE analysis. The same trends are captured, with the FE model predicting a more rapid increase of maximum displacement, which in turn, affects the energy release rate G shown in Fig. 6C. Once the vapor starved region is met, both models show the limit and reduction of the energy release rate. The nonlinear stress distribution is precisely captured as shown in the comparison for the u parameter in Fig. 6B. This shows that the bending and tensile stress reactions are developed similarly in both the FE model and the analytical model as the deformation increases due to a larger crack length or higher pressure. This excellent agreement gives strong confidence that the parametric analysis of vapor delamination in printed electronics can be carried out using the analytical framework described earlier.

The second FE model incorporating the meanders is shown in Fig. 6D–F and shows the crack growth as pressure is applied to the crack surfaces. In Fig. 6D, when the crack is just starting to grow as the void is pressurized, all deformation is elastic and reversable. In the next step Fig. 6E, the crack is just about to grow on the inner edge as the pressure has increased to 0.92 p_{sat} and the inside edge and outside edge have energy release rates of 29.7 and 27.9 J/m^2, respectively. These values are larger than both the first FE model and analytical model, where the predicted energy release rates are 25.3 and 20.5 J/m^2, respectively. This difference may be due to the presence of the silver interconnect, and the 'elastic hinge' boundary formed between the edge of the thin film and the bulk rather than the fixed boundary condition in both the analytical model and first FE model. The theoretical meander model in (17) estimates that the energy release rate on the inner face, G_i, to be 8.7 % larger than G_o, and the FE analysis calculates that it is 6.5 % larger. Fig. 6F then shows the progressive growth of the crack where the preferential direction is on the inside edge. The plastic strain after crack growth is through the thickness of the top PI layer, indicating significant plastic deformation, but not enough to rupture the blister. Despite the added complexity of the meander FE model, the close agreement between the absolute and relative values of G_i and G_o lend confidence to both the analytical model and the theoretical meander model developed in this paper.

3.7. Design implications

Several important design guidelines come out of the results discussed in previous sections. Careful design of the geometry of the printed interconnections, the fabrication process parameters, and the materials all have an impact on reducing the likelihood of delamination. Geometric design guidelines along with insights related to process parameters and material choice can be elucidated from the geometric parameter models investigated in this paper. Design guidelines to mitigate vapor driven delamination are highlighted below:

- Reduce moisture availability by
    - Reducing thickness of the bottom encapsulant layer
    - Incorporating a drying step before final cure in oven
    - Utilizing encapsulant with low moisture uptake
- Reduce width of printed nanoparticle-based traces to decrease the initial crack length
- Increase the thickness of the top layer of encapsulant layer
- Increase the meander radius, and
- Decrease the curing/sintering temperature

Reducing the moisture available is the most effective way to mitigate vapor driven delamination in flexible and stretchable electronics, and can be addressed with geometric design, process design, and material choices. Introducing a drying step or slow temperature ramp is perhaps the most easily implemented design change to reduce moisture availability, as it only requires simple oven temperature control and a short time period to drive off moisture before reaching the final curing or sintering temperature. Reducing the width of the printed nanoparticle-based trace is a geometric design parameter that can be changed to address delamination, but design changes in the conductor geometry may affect the electrical performance. If possible, conductor cross sections with higher aspect ratio will decrease the likelihood of vapor driven delamination while maintaining required electrical conductance. Increasing the thickness of the top polymer layer is another geometric design consideration as the increased bending resistance reduces the energy release rate for smaller cracks where the bending stresses dominate. However, increasing the thickness of the top polymer layer also increases the thermoelastic driven energy release rate. Increasing the meander radius can also mitigate delamination, but also impacts the areal footprint of the interconnection and can impact conductor densities. Decreasing the sintering/curing temperature will significantly reduce the maximum vapor pressure and proportionally reduce the thermoelastic strain to drive delamination. However, changing the sintering temperature may limit choice of material for the conductor or the sintering method [49] and may affect the mechanical and electrical properties of the interconnect. These considerations will help the flexible and stretchable electronics industry as this field moves increasingly from research phase to production.

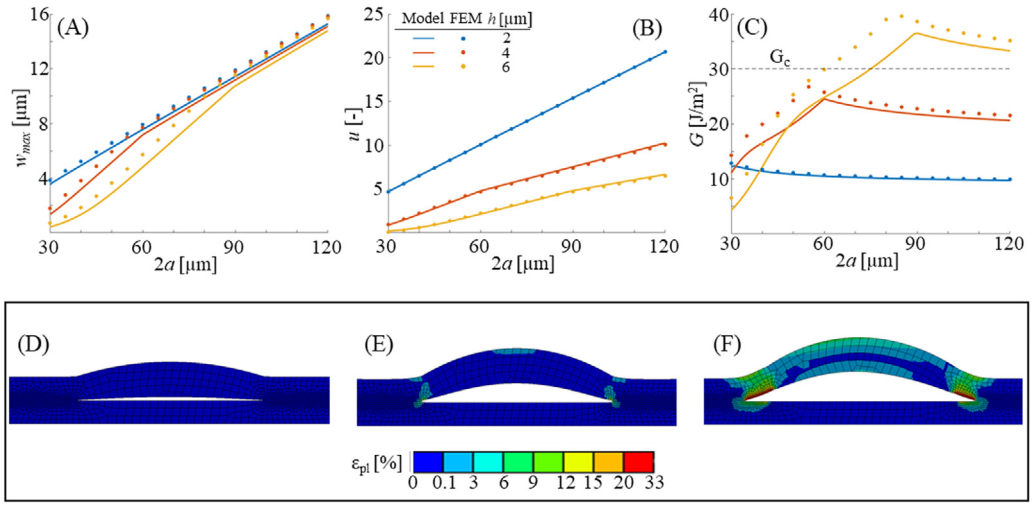

Fig. 6. Finite element model results and comparison with analytical model. (A–C) Compares the analytical model to the direct comparison FE model. (A) Comparison of the maximum displacement w_{max} at the center of the blister. (B) Comparison of the u factor, which determines whether the deformation behavior in the blister is membrane or plate dominated. (C) Comparison of the energy release rate development between the two models also showing the critical energy release rate of 30 J/m^2. (D–F) Results of the progressive crack growth model with meander geometry. Growth of the crack is shown in (D–F) for a PI thickness of 6 µm and silver width of 50 µm where (D) the crack is just opening due to a lower pressure, (E) the crack is just about to grow, and (F) the crack has preferentially grown towards the inside edge. The energy release rate just before growth in (E) is $G_i = 29.7$ J/m^2 and $G_o = 27.9$ J/m^2. The plastic strain ε_{pl} is displayed by the color map and shows minor plastic strain just before crack growth (E) and not completely through the thickness of the top PI; contrasting with (F) where plastic strain has occurred across the thickness of the PI after initial delamination. (For interpretation of the references to color in this figure legend, the reader is referred to the web version of this article.)

4. Conclusion

Delamination is observed in a 3D printed flexible electronic platform between two polymer layers, with a nanoparticle-based metallic interconnect acting as the crack initiation site. This problem is analyzed using a nonlinear fracture model with vapor pressure as the driving force for delamination. The results from the analytical model are consistent with experimental observations and are verified through FE modeling. The parametric model gives 'delamination mechanism maps' for flexible and stretchable electronics where two regimes described as vapor rich and vapor starved control the delamination. Transitioning from the vapor rich to vapor starved region, the energy release rate is limited and dominated by the moisture availability rather than the top film thickness and initial crack size. Designing a flexible and stretchable interconnection geometry and process in the vapor starved regime is therefore critical in reducing the likelihood of delamination. Delamination mechanism maps and design guidelines are presented to reduce the energy release rate in both vapor pressure and thermoelastic driven delamination. The metallic interconnection width is shown to be the second most critical dimension by both experimental observation and parametric model as the energy release rate can be reduced by 77 % when the metallic width is reduced from 50 µm to 30 µm when all other parameters are kept the same. Meander geometries are also investigated via a perturbation of the straight crack model, and the inside edge of the meander is shown to have a higher energy release rate when compared to the outside edge. These results provide important design considerations for improving the reliability of printed flexible and stretchable electronic devices.

Declaration of competing interest

The authors declare that they have no known competing financial interests or personal relationships that could have appeared to influence the work reported in this paper.

Acknowledgments

The authors gratefully acknowledge research funding from Highmark Health, Pittsburgh, and partial support from National Science Foundation grant #CMMI-1757117.

Appendix A. Supplementary data

Supplementary Information related to this article can be found online at https://doi.org/10.1016/j.eml.2021.101199.

References

[1] N. Matsuhisa, et al., Printable elastic conductors with a high conductivity for electronic textile applications, Nature Commun. 6 (2015) 7461.
[2] G.W. Huang, H.M. Xiao, S.Y. Fu, Wearable electronics of silver-nanowire/poly(dimethylsiloxane) nanocomposite for smart clothing, Sci. Rep. 5 (2015) 13971.
[3] S.P. Lee, et al., Highly flexible, wearable, and disposable cardiac biosensors for remote and ambulatory monitoring, NPJ Digit. Med. 1 (2018) 2.
[4] R. Herbert, et al., Fully printed, wireless, stretchable implantable biosystem toward batteryless, real-time monitoring of cerebral aneurysm hemodynamics, Adv. Sci. (Weinh) 6 (18) (2019) 1901034.
[5] J.A. Rogers, R. Ghaffari, D.-H. Kim, Stretchable Bioelectronics for Medical Devices and Systems, Springer, Switerland, 2016.
[6] C. Majidi, Soft robotics: A perspective—Current trends and prospects for the future, Soft. Robotics 1 (1) (2014) 5–11.
[7] X. Wang, R. Guo, J. Liu, Liquid metal based soft robotics: Materials, designs, and applications, Adv. Mater. Technol. (2018).
[8] H.U. Chung, et al., Binodal, wireless epidermal electronic systems with in-sensor analytics for neonatal intensive care, Science 363 (6430) (2019).
[9] Y.L. Park, et al., Design and control of a bio-inspired soft wearable robotic device for ankle-foot rehabilitation, Bioinspir. Biomim. 9 (1) (2014) 016007.
[10] S. Xu, A. Jayaraman, J.A. Rogers, Skin sensors are the future of health care, Nature 571 (2019) 319–321.
[11] Y. Khan, et al., Flexible hybrid electronics: Direct interfacing of soft and hard electronics for wearable health monitoring., Adv. Funct. Mater. 26 (47) (2016) 8764–8775.
[12] M.T. Rahman, et al., High performance flexible temperature sensors via nanoparticle printing., ACS Appl. Nano Mater. 2 (5) (2019) 3280–3291.
[13] L.J. Deiner, T.L. Reitz, Inkjet and aerosol jet printing of electrochemical devices for energy conversion and storage, Adv. Energy Mater. 19 (7) (2017).

[14] Q. Jing, et al., Freestanding functional structures by aerosol-jet printing for stretchable electronics and sensing applications., Adv. Mater. Technol. 4 (7) (2019).
[15] E. Suhir, An approximate analysis of stresses in multilayered elastic thin films, J. Appl. Mech. 55 (1988) 143–148.
[16] N. Naserifar, P.R. LeDuc, G.K. Fedder, Material gradients in stretchable substrates toward integrated electronic functionality, Adv. Mater. 28 (18) (2016) 3584–3591.
[17] A. Chowdhury, et al., The Effect of die attach layer delamination on the thermal performance of plastic packages, in: IEEE Electronic Components and Technology Conference, 1998.
[18] M. Kitano, A. Nishimura, S. Kawai, Analysis of package cracking during reflow soldering process, in: 26th Annual Proceedings Reliability Physics Symposium 1988, IEEE, 1988.
[19] H.B. Fan, M.M.F. Yuen, A multi-scale approach for investigation of interfacial delamination in electronic packages, Microelectron. Reliab. 50 (7) (2010) 893–899.
[20] Y.-Y. Hsu, et al., Polyimide-enhanced stretchable interconnects: Design, fabrication, and characterization., IEEE Trans. Electron Devices 58 (8) (2011) 2680–2688.
[21] M.V. Hoang, H.-J. Chung, A.L. Elias, Irreversible bonding of polyimide and polydimethylsiloxane (PDMS) based on a thiol-epoxy click reaction, J. Micromech. Microeng. 26 (10) (2016).
[22] C.H. Lee, et al., Soft core/shell packages for stretchable electronics, Adv. Funct. Mater. 25 (24) (2015) 3698–3704.
[23] J.-H. Jou, et al., Adhesion of polyimide to silicon and polyimide, J. Appl. Polym. Sci. 47 (1993) 1219–1232.
[24] X.J. Fan, et al., A micromechanics-based vapor pressure model in electronic packages, J. Electron. Packag. 127 (3) (2005) 262–267.
[25] D.C.C. Lam, J.I.T. Chong, T. Pin, The role of water in delamination in electronics packages: water evaporation from epoxy, IEEE Trans. Compon. Packag. Technol. 25 (4) (2002) 708–713.
[26] X. Zhang, et al., Effect of thermal misfit stress on steam-driven delamination in electronic packages, Eng. Fract. Mech. 194 (2018) 61–72.
[27] E.H. Andrews, A. Stevenson, Fracture energy of epoxy resin under plane strain conditions, J. Mater. Sci. 13 (1978) 1680–1688.
[28] K.M. Liechti, A. Shirani, Large scale yielding in blister specimens, Int. J. Fract. 67 (1994) 21–36.
[29] D.A. Dillard, Y. Bao, The peninsula blister test: A high and constant strain energy release rate fracture specimen for adhesives, J. Adhes. 33 (4) (2006) 253–271.
[30] B. Audoly, Stability of straight delamination blisters, Phys. Rev. Lett. 83 (1999).
[31] D. Xu, K.M. Liechti, T.H. de Lumley-Woodyear, Closed form nonlinear analysis of the peninsula blister test, J. Adhes. 82 (8) (2006) 831–866.
[32] M.G. Allen, S.D. Senturia, Application of the island blister test for thin film adhesion measurement, J. Adhes. 29 (1–4) (1989) 219–231.
[33] D.C.C. Lam, I.T. Chong, P. Tong, Parametric analysis of steam driven delamination in electronics package, IEEE Trans. Electron. Packag. Manuf. 23 (2000) 208–213.
[34] D.Z. Tansel, et al., Mechanical characterization of polydimethylsiloxane (PDMS) exposed to thermal histories up to 300 °C in a vacuum environment, J. Micromech. Microeng. 30 (6) (2020).
[35] M.T. Rahman, et al., 3D Printed high performance strain sensors for high temperature applications, J. Appl. Phys. 123 (2) (2018) 024501.
[36] M.T. Rahman, et al., Microscale additive manufacturing and modeling of interdigitated capacitive touch sensors, Sensors Actuators A 248 (2016) 94–103.
[37] S. Binder, M. Glatthaar, E. Rädlein, Analytical investigation of aerosol jet printing, Aerosol Sci. Technol. 48 (9) (2014) 924–929.
[38] G. Chen, et al., The effect of droplet sizes on overspray in aerosol-jet printing, Adv. Energy Mater. 20 (8) (2018).
[39] A. Mahajan, C.D. Frisbie, L.F. Francis, Optimization of aerosol jet printing for high-resolution, high-aspect ratio silver lines, ACS Appl. Mater. Interfac. 5 (11) (2013) 4856–4864.
[40] E.B. Secor, Principles of aerosol jet printing, Flex. Print. Electron. 3 (3) (2018).
[41] Dupont, Kapton: Summary of Properties, 2017.
[42] HDMicroSystems, Product Bulletin: PI 2525, PI 2555 & PI 2574, 2012.
[43] H.R. Brown, et al., Diffusion and self-adhesion of the polyimide PMDA-ODA, Polymer 29 (10) (1988) 1807–1811.
[44] M. Sadeq Saleh, et al., Polycrystalline micropillars by a novel 3-D printing method and their behavior under compressive loads, Scr. Mater. 149 (2018) 144–149.
[45] L.B. Freund, S. Suresh, Delamination and fracture, in: Thin Film Materials, Stress, Defect Formation and Surface Evolution, Cambridge University Press, Cambridge, UK, 2003, pp. 220–311.
[46] D. Denton, et al., Moisture diffusion in poltimide films in integrated circuits., J. Electron. Mater. 14 (2) (1985) 119–136.
[47] E. Sacher, J.R. Susko, Water permeation of polymer films. I. Polyimide, J. Appl. Polym. Sci. 23 (1979) 2355–2364.
[48] S. Timoshenko, S. Woinowski-Krieger, Theory of Plates and Shells, second ed., McGraw-Hill Book Company, 1959.
[49] R. Danaei, et al., Ultrafast fabrication of thermoelectric films by pulsed light sintering of colloidal nanoparticles on flexible and rigid substrates., Adv. Energy Mater. 21 (1) (2019) 1800800.